Ductile damage analysis under extreme low-cycle biaxial shear loadings: Experiments and simulations

Zhichao Wei [a,b],[*], Marleen Harting [a], Steffen Gerke [a], Michael Brünig [a]

[a] Institut für Mechanik und Statik, Universität der Bundeswehr München, Werner-Heisenberg-Weg 39, D-85577 Neubiberg, Germany
[b] Institute of Metal Forming, RWTH Aachen University, Intzestr. 10, D-52072 Aachen, Germany

ARTICLE INFO

ABSTRACT

This paper addresses the experimental and numerical analysis of ductile damage under extremely low-cycle loading conditions with a large strain range. Shear cyclic loading stress states with stress triaxiality of approximately zero are generated using the biaxially loaded cruciform X0-specimen, with equal positive and negative forces applied to different loading axes. Monotonic and various symmetric cyclic loading patterns are designed to investigate the influence of loading histories on the material response at both macro- and micro-levels. The numerical calculations are performed using a novel anisotropic continuum damage model. For plasticity, the hydrostatic sensitivity Drucker–Prager yield condition with combined hardening is used to characterize the isotropic plastic behavior. Additionally, an anisotropic damage strain tensor that considers stress state influences is used to predict the occurrence and development of damage. Digital image correlation (DIC) technique and scanning electron microscopy (SEM) technique enable comparison of experimental and numerical results in different aspects. The numerical results for load–displacement curves, total strain field, and damage strains agree well with the experimental data, as confirmed by quantitative error analysis in load–displacement curves and statistical analysis of SEM images.

1. Introduction

Ductile damage analysis is essential in engineering structures to prevent accidents and enhance material efficiency in the design process. A large number of experimental observations have confirmed that ductile damage depends on different stress states (Bao and Wierzbicki, 2004; Brünig et al., 2008; Weck and Wilkinson, 2008; Gao et al., 2010; Voyiadjis et al., 2012; Mohr and Marcadet, 2015; Wei et al., 2022; Wu et al., 2022). Damage is caused by the nucleation, growth and coalescence of micro-voids under high stress triaxialities. In contrast, shear-dominated loading with zero or low negative stress triaxialities induces the growth and coalescence of micro-shear-cracks, leading to failure. In addition, low positive stress triaxialities result in mixed damage mechanisms due to micro-defects (micro-voids and micro-shear cracks) growth and coalescence. Different researchers (Bao and Wierzbicki, 2005; Khan and Liu, 2012; Brünig et al., 2018) have discussed the cut-off values for negative stress triaxialities, where no damage is observed. Among them, Brünig et al. (2016) analyzed experimental and numerical biaxial shear-compression tests, adjusting the cut-off value to −0.6 and indicating that this cut-off value also depends on the Lode parameter.

The occurrence and development of ductile damage are also significantly influenced by loading paths or histories. Non-proportional monotonic loading and cyclic loading conditions are discussed in the literature. Loading changes for tension-torsion in cylindrical specimens or tension-shear in cruciform biaxially loaded specimens are commonly studied by various researchers (Papasidero et al., 2015; Cortese et al., 2016; Iftikhar and Khan, 2021; Brünig et al., 2021; Zistl et al., 2022; Hou et al., 2022; Raj et al., 2022; Kong et al., 2023). Their results show that different loading sequences and preload magnitude significantly alter material behavior. For example, Brünig et al. (2021) indicates that a non-proportional loading path change from shear to tension decreases the ductility of the investigated aluminum alloy. Pre-compression loading enhances the fracture strain after changing to shear loading, as discussed by Papasidero et al. (2015). In addition, as shown in Kong et al. (2023), only large pre-tension loading can significantly affect material ductility in tension-to-shear loading conditions.

Furthermore, one-axis cyclic loading has been widely discussed in previous work (Yoshida et al., 2002; Barlat et al., 2003; Kanvinde and Deierlein, 2007; Shi et al., 2011; Faleskog and Barsoum, 2013; Voyiadjis et al., 2013; Marcadet and Mohr, 2015; Algarni et al.,

2019; Wei et al., 2022; Wu et al., 2024), including uniaxial tension-compression, one-axis shear, and uniaxial torsion cyclic tests. Kanvinde and Deierlein (2007) performed several low-cycle loading experiments and observed that deformed micro-voids under compression loading conditions may more easily coalesce with neighboring deformed flat penny-shaped micro-voids under tension reversal loading conditions. In addition, damage develops rapidly in the early loading cycles until it reaches a critical state, after which it evolves more slowly (Algarni et al., 2019). One limitation of those mentioned above one-axis cyclic loading is that it generates only very specific stress states. To address this issue, Wei et al. (2023a,b, 2024a) designed a series of biaxial cyclic loading experiments using HC-specimens, generating a wide range of stress triaxialities. Their experimental and numerical results clearly indicate how stress states affect material behavior under reverse loading conditions; for example, pre-compression loading increases material ductility, whereas pre-tension reduces the ductility of the investigated aluminum alloy. Moreover, the investigation of single-cycle and bi-cycle biaxial experiments highlighted the effect of loading patterns and histories on damage behavior.

It is worth noting that all current biaxial reverse loading experiments refer only to twice-reversed loading. Considering the number of loading cycles, the influence of damage behavior has yet to be thoroughly discussed. However, in the present work, fatigue damage caused by very small loading ranges, resulting in small plastic deformation in each loading cycle and failure by strain localization, is not detected. Thus, the number of loading cycles is limited to a specific value, and ductile damage leads to failure under large plastic deformations. Moreover, the newly designed experiments should also be able to extend across a wide range of stress triaxialities in the future; therefore, one-axis-loaded experiments are not considered. Considering all factors, biaxially loaded specimens subjected to various large strain ranges are introduced in the present work. Achieving shear loading (with stress triaxiality and Lode parameter nearly zero and within a small tolerance) remains challenging for metal sheet specimens. Several challenges must be addressed, including reaction moments in one-sided shear tests (Bouvier et al., 2006), potential rotation under large deformations (Driemeier et al., 2010), the need for specialized testing machines (Brosius et al., 2011; Dunand and Mohr, 2011), buckling tendency under reverse loading, and non-zero stress triaxiality and Lode parameters (Brünig et al., 2022). To address these issues, the biaxially loaded X0-specimen proposed by Gerke et al. (2017), which applies equal positive and negative stress along different loading axes, is a practical testing specimen. This setup generates a near-zero stress state and allows for a broad range of stress states by adjusting different loading ratios in future studies.

A shear-dominated damage mechanism is one of the limitations of the original Gurson model, as it only considers the growth of voids (Gurson, 1977). Although the Gurson model has been extensively modified to predict shear-dominated damage mechanism (Tvergaard and Needleman, 1984; Nahshon and Hutchinson, 2008; Xue et al., 2013; Zhou et al., 2014; Malcher et al., 2014; Khan et al., 2023; Wu et al., 2022), it cannot account for the degradation of Young's modulus due to damage. Additionally, damage models based on a scalar damage variable cannot capture the anisotropic deformations in different directions of micro-defects, among others (Lemaitre, 1985; Lian et al., 2013; Zhang et al., 2023; Zeng et al., 2024; Zhang et al., 2025). The damage tensor provides a practical approach to modeling anisotropic damage properties (Chaboche, 1992; Hayakawa et al., 1998; Voyiadjis and Kattan, 1999; Abu Al-Rub and Voyiadjis, 2003; Voyiadjis and Kattan, 2005, 2009). Therefore, in the present work, the damage strain rate tensor proposed by Brünig (2003) is used to characterize the volume and shape changes of micro-defects and the damage tensor is incorporated into Kirchhoff stress tensor (Hayakawa et al., 1998; Brünig, 2003) to model the degradation of elastic properties. Recently, Wei et al. (2022, 2023b, 2024c) incorporated the Bauschinger effect, stress-differential effect (Spitzig and Richmond, 1984; Holmen

Table 1
Chemical composition of the aluminum alloy EN-AW 6082-T6 (AlSiMgMn) (Wei et al., 2022).

Al	Si	Mg	Mn	Fe
to balance	0.90%	0.70%	0.47%	0.37%
	Cu	**Zn**	**Ti**	**Others**
	0.09%	0.09%	0.03%	0.06%

et al., 2017), and non-hardening effect (Ohno, 1982; Daroju et al., 2022) into Brünig's model (Brünig, 2003) and introduced the concept of a kinematic softening law, based on the proposed damage strain rate tensor, to predict changes in the damage surface under cyclic loading conditions. The proposed model has been sufficiently verified under various complex loading conditions covering a wide range of stress states. The numerical results align well with the experimental data at both macro- and micro-levels.

In this paper, the structure is organized as follows. Section 2 describes the investigated material, specimen, and testing program. Section 3 summarizes the proposed material model. The numerical setup is introduced in Section 4. An analysis of the experimental and numerical results, including the global load–displacement curve, DIC measured strain field, predicted damage strain, and SEM images, is presented in Section 5. Conclusions are provided in Section 6.

2. Material, specimen and experiments

This study uses aluminum EN-AW 6082-T6, which has been extensively investigated in recent years by our research group (see Wei et al. 2022, 2023a, 2024a). It is highly interested in industries due to its excellent welding and machining properties. Additionally, it is suitable for testing because of its stable material properties, making it ideal for studying damage and fracture behavior. The chemical property is shown in Table 1.

Compared to previous studies, the X0-specimen is used in these newly designed biaxial cyclic loading experiments, replacing the HC-specimen, as it generates the same stress states in both the horizontal and vertical directions. As indicated in Gerke et al. (2017) and Wei et al. (2023a), tension/compression or shear stress states are induced when loads are applied in the horizontal and vertical directions of the HC-specimen, respectively. However, as shown in Fig. 1, the X0-specimen features four bi-symmetric notches at a 45° angle to the axes. This design results in more uniform deformations along both axes compared to the HC-specimen. In addition, the central hole of the X0-specimen resembles a flower, giving it the name X0-flower (see Figs. 1 (b) and (c)). Moreover, tensile stress triaxialities with high hydrostatic stress states are generated when both axes are subjected to the same tensile loads, while a shear-dominant stress state arises when a tensile load is applied to one axis and a compressive load is applied to the other. It is evident that the X0-specimen can also cover a wide range of stress states by varying the loads on the axes.

One of the highlights of this work is the application of different numbers of cyclic loads to the X0-specimens with a thickness 4 mm, extending beyond the 1.5 loading cycles investigated in previous studies (Wei et al., 2023a, 2024a). In addition, Wei et al. (2022) analyzed the experimental and numerical results of one-axial tension–compression and shear cyclic experiments, observing that increased loading cycles led to a decrease in ductility in the studied aluminum alloy. Moreover, the one-axis-loaded shear specimen generated a stress triaxiality of approximately 0.1 (Wei et al., 2022). However, the X0-specimen induces a near-zero stress state when positive and negative loads are applied on the vertical and horizontal axes (Gerke et al., 2017), respectively, i.e., so-called loading case $\zeta = 1/-1$. This setup allows for a more accurate study of shear-dominated damage and fracture under different cyclic loading conditions. It is important to emphasize that the proposed cyclic experiments focus on large strain ranges, resulting in ductile damage and fracture under cyclic loading conditions.
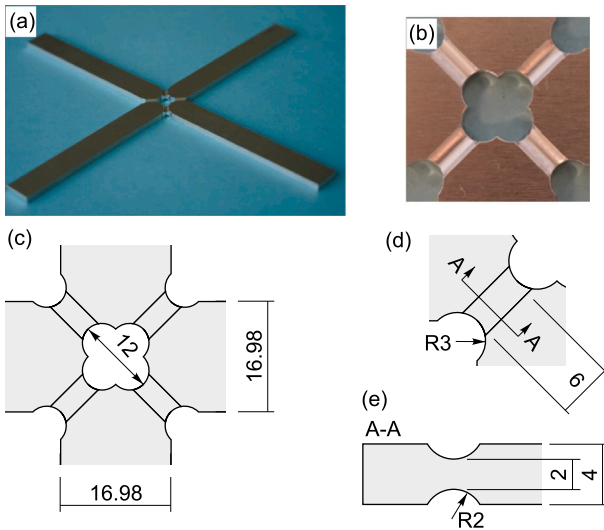
Fig. 1. Sketch of the X0-specimen, all units in mm: (a) isometric photo of the overview for the X0-specimen, (b) isometric photo of the central notched X0-flower, (c) and (d) details of the central notched X0-flower, and (e) cross-section A–A of the notch part. The length of both axes is 240 mm and the thickness is 4 mm.

Table 2
DIC analysis parameters.

DIC software	Istra 4D (Dantec Dynamics)
Region of interest (ROI)	2752 × 2206 pixels
Subset (facet size)	33 × 33 pixels
Grid spacing (overlap)	11 × 11 pixels
Alignment	Object
Reference	Plane
Rung step	Every thirty steps
Contour smoothing	None
Displacement smoothing	None

2.1. Experimental setups

All tests are performed under static loading conditions at a machine speed of 0.004 mm/s using a horizontally arranged electromechanical biaxial testing machine (LFM-BIAX) manufactured by Walter+Bai, Switzerland. Overall, the tests showed very good reproducibility in the load–displacement behavior and the number of loading cycles. The downholder is additionally employed to restrict deformation in the thickness direction and prevent early buckling under compressive loading conditions (Gerke et al., 2024; Wei et al., 2024a). Instead of the traditional extensometer measurement, the digital image correlation technique (DIC) records and analyzes data during the experiments. To achieve this, two 6 Mpx cameras with 75 mm lenses are positioned above the X0-specimen, accompanied by sufficient side LED lighting to capture high-quality images. The camera frequency is adjusted to 1 Hz. The commercial software Istra 4D (Dantec Dynamics) is used to analyze the experimental results, and the evaluation parameters are shown in Table 2.

After fracture, the specimen surfaces are examined using the ZEISS EVO 15 scanning electron microscopy (SEM) to analyze the microstructure under different cyclic loading conditions, focusing on the distribution and types of micro-defects. The details of the ZEISS EVO 15 are summarized in Table 3.

2.2. Testing methodology

To subject the X0-specimen to different numbers of loading cycles, five distinct loading patterns are considered, with machine displacements of u_2^M at ∓ 0.55 mm, ∓ 0.65 mm, ∓ 0.8 mm, ∓ 1.0 mm, and ∓ 1.2 mm. In previous monotonic biaxial tests with a loading case of $\zeta =$

Table 3
SEM technical parameters.

SEM equipment	ZEISS EVO 15
Emitter	Lanthanum hexaboride (LaB6)
Detector	Everhart-Thornley (ET) detector
Working environment	High vacuum
Working distance	11 mm
Electron beam diameter	300 nm
Accelerating voltage	20 kV

Table 4
Test classification for the biaxial experiments with X0-specimen.

Tests ID	Loading patterns	ζ	u_2^M till [mm]	κ^M [%]
X0-mon-(1/-1)	monotonic	1/-1	fracture	100
X0-cyc-(1/-1)-1.2	cyclic	1/-1	∓ 1.2	92
X0-cyc-(1/-1)-1.0	cyclic	1/-1	∓ 1.0	77
X0-cyc-(1/-1)-0.8	cyclic	1/-1	∓ 0.8	62
X0-cyc-(1/-1)-0.65	cyclic	1/-1	∓ 0.65	50
X0-cyc-(1/-1)-0.55	cyclic	1/-1	∓ 0.55	42

$1/-1$, the maximum compressive machine displacement u_2^M observed in the horizontal axis (axis 2, see Fig. 3) for the X0-specimen was approximately -1.3 mm. Therefore, the loading ratios based in machine displacement (κ^M) relative to the maximum loading capacity are 42%, 50%, 62%, 77%, and 92%, respectively. In this paper, the test is named X0-mon/cyc-(1/-1)-x, where X0 refers to the testing specimen, mon and cyc indicate monotonic and cyclic loading, respectively, (1/-1) denotes the force ratio, and x describes the absolute machine displacement u_2^M for each loading pattern in the horizontal axis (axis 2). Following this naming convention, the newly designed tests are labeled as: X0-mon-(1/-1), X0-cyc-(1/-1)-0.55, X0-cyc-(1/-1)-0.65, X0-cyc-(1/-1)-0.8, X0-cyc-(1/-1)-1.0, and X0-cyc-(1/-1)-1.2. The details are summarized in Table 4.

The designed testing routine is as shown in Fig. 2. During the experiments, cylinders 2.1, 1.2, and 2.2 are controlled by displacement, whereas cylinder 1.1 is force-driven to achieve a loading ratio of $\zeta = F_1/F_2 = 1/-1$ (coordinate see Fig. 3). For monotonic loading, $u_{2.1}^M$ is set large enough to cause failure. In addition, the input machine displacements are shown in Table 4 for the other cyclic loading cases.

Moreover, the mean displacements and forces used during the experimental data evaluation and numerical analysis are defined as:

$$F_i = \frac{F_{i.1} + F_{i.2}}{2} \quad (i = 1, 2), \tag{1}$$

and

$$\Delta u_{\text{ref}.i} = u_{i.1} + u_{i.2} \quad (i = 1, 2), \tag{2}$$

respectively. The measure points and the force and displacement symbols are shown in Fig. 3.

3. Phenomenological cyclic plastic-damage model

This section outlines the basic formulations of the cyclic isotropic plasticity and anisotropic damage model used for the experimental-numerical analysis of newly designed shear-dominated biaxial cyclic experiments. In the proposed continuum damage model, undamaged configurations represent the material in its undamaged state and damaged configurations that characterize the elastic–plastic deformed and damaged state. The mapping between the undamaged and damaged configurations is described in terms of the damage tensor. Furthermore, the logarithmic damage strain tensor is calculated from the damage tensor and integrated into Hooke's law to determine the Kirchhoff stress of the damaged material in the damaged configurations. A detailed description of the framework of the present theory can be found in Wei et al. (2024c, 2023a).
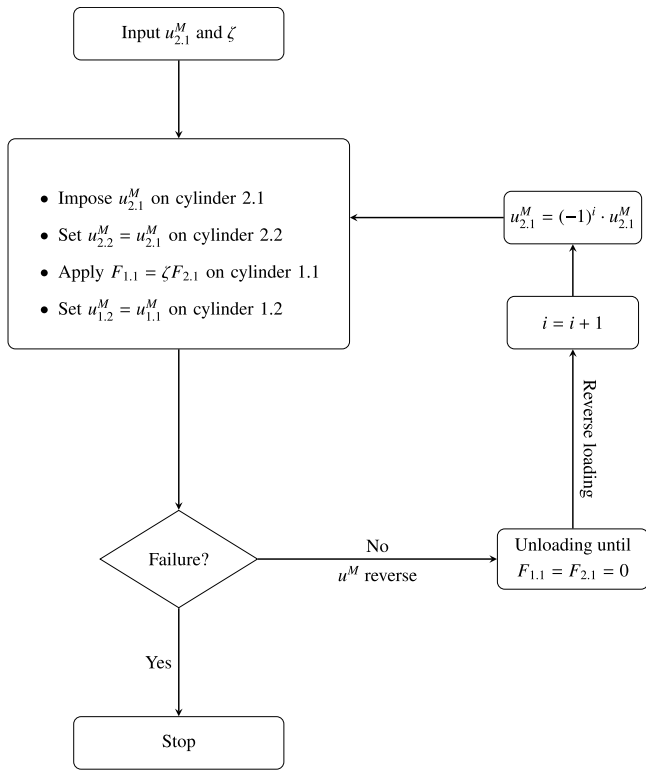
Fig. 2. Flowchart for machine testing routine. Note that the initial value of i is set to zero.
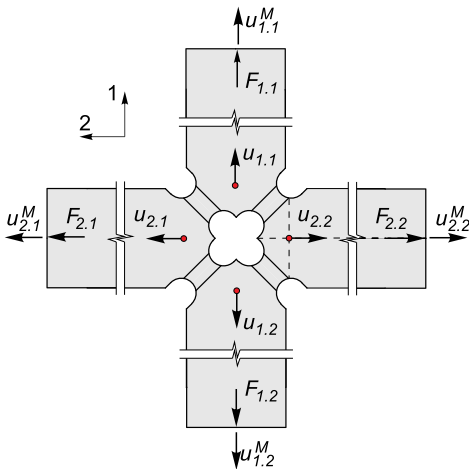

Fig. 3. Sketch of forces and displacements.

3.1. Cyclic plastic model

The Drucker–Prager yield surface is expressed as (Wei et al., 2023a)

$$f^{\mathrm{pl}} = \sqrt{\frac{1}{2}\mathrm{dev}(\bar{\mathbf{T}} - \bar{\boldsymbol{\alpha}})\cdot\mathrm{dev}(\bar{\mathbf{T}} - \bar{\boldsymbol{\alpha}})} - \bar{c}\left(1 - \frac{a}{\bar{c}}\mathrm{tr}(\bar{\mathbf{T}} - \bar{\boldsymbol{\alpha}})\right)$$
$$= \sqrt{\bar{J}_2} - \bar{c}(1 - \frac{a}{\bar{c}}\bar{I}_1) = 0, \tag{3}$$

where $\bar{\mathbf{T}}$ is the effective Kirchhoff stress tensor, $\bar{\boldsymbol{\alpha}}$ describes the effective back stress tensor, $\bar{c}$ denotes the effective equivalent stress, $a/\bar{c}$ represents the hydrostatic coefficient, and $\bar{I}_1$ and $\bar{J}_2$ are the first and second deviatoric effective reduced stress tensor ($\bar{\mathbf{T}}-\bar{\boldsymbol{\alpha}}$) invariants, respectively.

The effective Kirchhoff stress is calculated using isotropic Hooke's law

$$\bar{\mathbf{T}} = 2G\mathbf{A}^{\mathrm{el}} + \left(K - \frac{2}{3}G\right)\mathrm{tr}\,\mathbf{A}^{\mathrm{el}}\mathbf{1}, \tag{4}$$

where $\mathbf{A}^{\mathrm{el}}$ is the elastic strain tensor, $\mathbf{1}$ denotes the second order identity tensor, and G and K describe the shear and bulk modulus, respectively

Furthermore, the plastic strain rate tensor $\dot{\mathbf{H}}^{\mathrm{pl}}$ is governed by

$$\dot{\mathbf{H}}^{\mathrm{pl}} = \dot{\lambda}\frac{1}{2\sqrt{\bar{J}_2}}\mathrm{dev}(\bar{\mathbf{T}} - \bar{\boldsymbol{\alpha}}) = \dot{\gamma}\bar{\mathbf{N}}, \tag{5}$$

with a scalar plastic multiplier $\dot{\lambda} = \sqrt{2}\dot{\gamma}$ and the effective deviatoric reduced stress direction $\bar{\mathbf{N}}$.

3.2. Anisotropic ductile damage model

The stress triaxiality η and the Lode parameter ω are introduced to capture the stress state. The stress triaxiality η is defined as the ratio of the mean stress σ_{m} to the von Mises equivalent stress σ_{eq},

$$\eta = \frac{\sigma_{\mathrm{m}}}{\sigma_{\mathrm{eq}}} = \frac{I_1}{3\sqrt{3J_2}} = \frac{\mathrm{tr}(\mathbf{T})}{\sqrt{\frac{27}{2}\mathrm{dev}\mathbf{T}\cdot\mathrm{dev}\mathbf{T}}}, \tag{6}$$

where I_1 and J_2 are the first and second deviatoric stress invariants, and $\mathbf{T}$ represents the Kirchhoff stress tensor. In addition, the Kirchhoff stress can be computed in the form of

$$\mathbf{T} = 2(G + \eta_2\mathrm{tr}\mathbf{A}^{\mathrm{da}})\mathbf{A}^{\mathrm{el}} + \left[(K - \frac{2}{3}G + 2\eta_1\mathrm{tr}\mathbf{A}^{\mathrm{da}})\mathrm{tr}\mathbf{A}^{\mathrm{el}}\right.$$
$$\left. + \eta_3(\mathbf{A}^{\mathrm{da}}\cdot\mathbf{A}^{\mathrm{el}})\right]\mathbf{1} + \eta_3\mathrm{tr}\mathbf{A}^{\mathrm{el}}\mathbf{A}^{\mathrm{da}} + \eta_4(\mathbf{A}^{\mathrm{el}}\mathbf{A}^{\mathrm{da}} + \mathbf{A}^{\mathrm{da}}\mathbf{A}^{\mathrm{el}}), \tag{7}$$

where $\mathbf{A}^{\mathrm{da}}$ represents the damage strain tensor and $\eta_1...\eta_4$ are elastic damage degradation parameters. It is evident that the elastic properties will be altered due to the evolution of damage.

Moreover, the Lode parameter

$$\omega = \frac{2T_2 - T_1 - T_3}{T_1 - T_3} \tag{8}$$

is defined based on the principal stresses T_1, T_2, and T_3.

In addition, the damage condition characterizes the onset of damage, taking into account different stress states (Wei et al., 2023a)

$$f^{\mathrm{da}} = \hat{\alpha}\,\mathrm{tr}(\mathbf{T} - \boldsymbol{\alpha}) + \hat{\beta}\sqrt{\frac{1}{2}\mathrm{dev}(\mathbf{T} - \boldsymbol{\alpha})\cdot\mathrm{dev}(\mathbf{T} - \boldsymbol{\alpha})} - \tilde{\sigma}$$
$$= \hat{\alpha}I_1 + \hat{\beta}\sqrt{J_2} - \tilde{\sigma} = 0, \tag{9}$$

where $\hat{\alpha}(\eta,\omega)$ and $\hat{\beta}(\eta,\omega)$ are stress-state-dependent variables (Brünig et al., 2013; Wei et al., 2023a), $\boldsymbol{\alpha}$ denotes the damage back stress tensor, and $\tilde{\sigma}$ describes the equivalent damage stress.

To characterize the stress-state-dependent damage evolution, the damage strain rate tensor is defined by

$$\dot{\mathbf{H}}^{\mathrm{da}} = \dot{\mu}(\tilde{\alpha}\frac{1}{\sqrt{3}}\mathbf{1} + \tilde{\beta}\tilde{\mathbf{N}}), \tag{10}$$

where $\dot{\mu}$ describes the scalar damage multiplier, $\tilde{\alpha}(\eta,\omega)$ and $\tilde{\beta}(\eta,\omega)$ are stress-state-dependent variables, and $\tilde{\mathbf{N}}$ represents the normalized transformed reduced stress tensor. The first part ($\dot{\mu}\tilde{\alpha}\frac{1}{\sqrt{3}}\mathbf{1}$) describes the volumetric deformation caused by the growth of micro-defects, while the deviatoric term ($\dot{\mu}\tilde{\beta}\tilde{\mathbf{N}}$) represents the isochoric deformation induced by micro-defects.

3.3. Hardening and softening laws

A detailed explanation of the selected hardening and softening laws is provided by Wei et al. (2022, 2023a). Firstly, the isotropic hardening component is formulated using the extended double-term Voce hardening model

$$\bar{c} = c_0 + Q_1(1 - e^{-p_1\gamma}) + Q_2\xi(1 - e^{-p_2\gamma}), \tag{11}$$

with exponential hardening law parameters $\{c_0, Q_1, Q_2, p_1, p_2, \xi\}$. Based on the experimental and numerical study of the hardening behavior in a wide range of strain states (Wei et al., 2023a), ξ is defined as

$$\xi = \begin{cases} -6.650\eta_{el} - 0.565 & \text{for} & \eta_{el} < -0.1 \\ \dfrac{1}{f_\xi} & \text{for} & -0.1 \leq \eta_{el} < 0.1 \text{ and } \eta_{el} \geq 0.45 \\ 2.477\eta_{el} + 1.025 & \text{for} & 0.1 \leq \eta_{el} < 0.45 \end{cases} \tag{12}$$

with

$$f_\xi = 0.787 \left(1 + e^{-50(\eta_{el}+1)}\right),$$

where η_{el} is the elastic strain triaxiality. It can be calculated based on the elastic strain tensor $\mathbf{A}^{el}$ as

$$\eta_{el} = \frac{\text{tr}\mathbf{A}^{el}}{\sqrt{\frac{3}{2}\text{dev}\mathbf{A}^{el} \cdot \text{dev}\mathbf{A}^{el}}}, \tag{13}$$

where $\text{tr}\mathbf{A}^{el}$ and $\text{dev}\mathbf{A}^{el}$ represent the isotropic and deviatoric parts of the elastic strain tensor, respectively.

The decomposed effective back stress rate tensors are

$$\dot{\bar{\boldsymbol{\alpha}}}_1 = b_1 \chi \dot{\mathbf{H}}^{pl} - b_2 \chi \dot{\gamma}\bar{\boldsymbol{\alpha}}_1, \quad \dot{\bar{\boldsymbol{\alpha}}}_2 = b_3 \dot{\mathbf{H}}^{pl} - b_4 \dot{\gamma}\bar{\boldsymbol{\alpha}}_2,$$

$$\dot{\bar{\boldsymbol{\alpha}}}_3 = b_5 \dot{\mathbf{H}}^{pl} - \left(1 - \frac{((\bar{\mathbf{T}} - \bar{\boldsymbol{\alpha}}) \cdot \bar{\boldsymbol{\alpha}}_3)^2}{\|\bar{\mathbf{T}} - \bar{\boldsymbol{\alpha}}\| \, \|\bar{\boldsymbol{\alpha}}_3\|}\right) b_6 \dot{\gamma}\bar{\boldsymbol{\alpha}}_3, \tag{14}$$

with the parameters $\{\chi, b_1, b_2, b_3, b_4, b_5, b_6\}$.

Secondly, the exponential isotropic softening law is given in the form of

$$\tilde{\sigma} = \tilde{\sigma}_0 - C_1 e^{-C_2 \mu}, \tag{15}$$

where the isotropic softening parameters $\{\tilde{\sigma}_0, C_1, C_2\}$ and μ is the equivalent damage strain. Moreover, the transformation of the damage surface is characterized by

$$\dot{\boldsymbol{\alpha}} = d_1 \dot{\mathbf{H}}^{da} - d_2 \dot{\mu}\boldsymbol{\alpha}, \tag{16}$$

with kinematic softening parameters $\{d_1, d_2\}$.

In addition, the scalar parameter $\rho_h = \rho_s = 0.41$ is introduced to incorporate both isotropic ($\dot{c}$) and kinematic hardening ($\dot{\boldsymbol{\alpha}}$), as well as isotropic ($\dot{\sigma}$) and kinematic softening ($\dot{\boldsymbol{\alpha}}_{eq}$), expressed as follows:

$$\begin{aligned} \dot{\tilde{\sigma}} &= \rho_h \dot{\tilde{c}} + (1 - \rho_h)\dot{\tilde{\alpha}} \\ \dot{\sigma} &= \rho_s \dot{\tilde{\sigma}} + (1 - \rho_s)\dot{\alpha}_{eq}, \end{aligned} \tag{17}$$

where $\dot{\tilde{\sigma}}$ and $\dot{\sigma}$ represent the effective equivalent stress rate and the equivalent stress rate, respectively.

It must be emphasized that the hardening parameters $\{c_0, Q_1, Q_2, p_1, p_2, \xi, \chi, b_1, b_2, b_3, b_4, b_5, b_6\}$ for the investigated aluminum have been directly or indirectly identified through uniaxial monotonic and cyclic tension-compression and shear tests. The fitting strategy is discussed by Wei et al. (2023c, 2024b). However, the softening parameters $\{\tilde{\sigma}_0, C1, C_2, d_1, d_2\}$ can be only inversely identified through micro-numerical simulations (Brünig et al., 2013; Wei et al., 2023a). The material parameters and descriptions used are shown in Table 5.

4. Numerical modeling

The proposed constitutive model has been implemented as a user-defined subroutine in ANSYS, and its numerical integration based on an efficient Euler explicit approach is detailed in Wei et al. (2024c). Previous numerical studies have demonstrated the robust stability of the algorithm under a variety of complex loading conditions (Wei et al., 2023b, 2024c,a). The convergence criterion for the global nonlinear analysis is set to the default value of 0.005 for force. In addition, 3D 8-node structural solid elements (SOLID185) are used in the numerical calculations.

Moreover, only one-fourth of the X0-specimen is modeled to predict the material response and save computational time due to its bi-symmetrical properties. As shown in Fig. 4, coarse elements are used outside the notch region, while a finer element size is applied within

Table 5
Plastic-damage material parameters.

Symbol	In Eq.	Description	Value	Unit
a/c	(3)	Hydrostatic stress coefficient	32	$1/\text{TPa}$
c_0	(11)	Initial yield stress	139	MPa
Q_1	(11)	Isotropic hardening modulus	74.93	MPa
Q_2	(11)	Isotropic hardening modulus	21.32	MPa
p_1	(11)	Isotropic hardening exponent	8.96	–
p_2	(11)	Isotropic hardening exponent	676.01	–
ξ	(11)	Stress state based variable function	See (12) and (13)	
ρ_h	(17)	Isotropic hardening ratio	0.41	–
b_1	(14)	Kinematic hardening modulus	61 250	MPa
b_2	(14)	Kinematic hardening constant	1750	–
b_3	(14)	Kinematic hardening modulus	895	MPa
b_4	(14)	Kinematic hardening constant	15	–
b_5	(14)	Kinematic hardening modulus	115	MPa
b_6	(14)	Kinematic hardening constant	7.5	–
χ	(14)	Exponential Decay function	$\chi = 0.8e^{-300\gamma} + 0.2$	
$\tilde{\sigma}_0$	(15)	Initial equivalent damage stress	290	MPa
C_1	(15)	Isotropic softening modulus	0.004207	MPa
C_2	(15)	Isotropic softening exponent	92.97	–
d_1	(16)	Kinematic softening modulus	−0.51	MPa
d_2	(16)	Kinematic softening constant	−84	–
ρ_s	(17)	Isotropic softening ratio	0.41	–

the notch region. The element size ($0.25\,\text{mm} \times 0.125\,\text{mm} \times 0.1\,\text{mm}$) in the notch region is the same as that of the HC-specimen in the numerical simulations, which also has the same notch dimensions. These meshes provide accurate and stable results across different loading conditions.

In addition, displacement control is used in the numerical simulations. One of the most challenging tasks is ensuring that the simulated load ratio ζ matches the experimentally designed value. In this work, a special iterative method is introduced to address this issue. Specifically, the applied displacement boundary condition Δu_2 on the horizontal axis is kept fixed, whereas the imposed displacement on the vertical axis is set as $\Delta u_1 = \zeta^{tr}\Delta u_2$ until the simulated force ratio, $\Delta F_1^{sim}/\Delta F_2^{sim}$, reaches -1. The trial value is initially assumed to be the same as in the previous load step for each new load step. If $\zeta^{sim} = \Delta F_1^{sim}/\Delta F_2^{sim} \neq -1$ with a tolerance of $\pm 0.5\%$, a new trial value is suggested to be calculated as follow:

$$\zeta^{tr} = \begin{cases} \zeta^{tr} - \dfrac{\zeta^{sim} - \zeta^{exp}}{m} & \text{for} & \zeta^{sim} < \zeta^{exp} \\ \zeta^{tr} - \dfrac{\zeta^{sim} - \zeta^{exp}}{m} & \text{for} & \zeta^{sim} > \zeta^{exp} \end{cases}, \tag{18}$$

where m may depend on the load step and is set to 200 in this context. Typically, two or three iterations are sufficient to determine the correct displacement boundary condition to achieve the desired loading ratio.

5. Result and discussion

This section analyzes the experimental results using the digital image correlation (DIC) technique and scanning electron microscopy (SEM) from various perspectives: the global load–displacement field, the local strain field, the macroscopic fracture behavior, and the microstructure of the fracture surfaces. Moreover, numerical calculations provide experimentally measurable load–displacement curves, strain distributions, and key information that cannot be directly measured, such as the local evolution of stress states and damage.

5.1. Displacements and strains

The experimental and numerical load–displacement curves are illustrated in Fig. 5, and the experimental results show good agreement with the numerical predictions in both axes. To quantitatively analyze the quality of the numerical results, the mean relative force error is introduced as

$$\bar{r}(F) = \frac{1}{n}\sum_{i=1}^{n}\left|\frac{F_i^{sim} - F_i^{exp}}{F_i^{exp}}\right|, \tag{19}$$
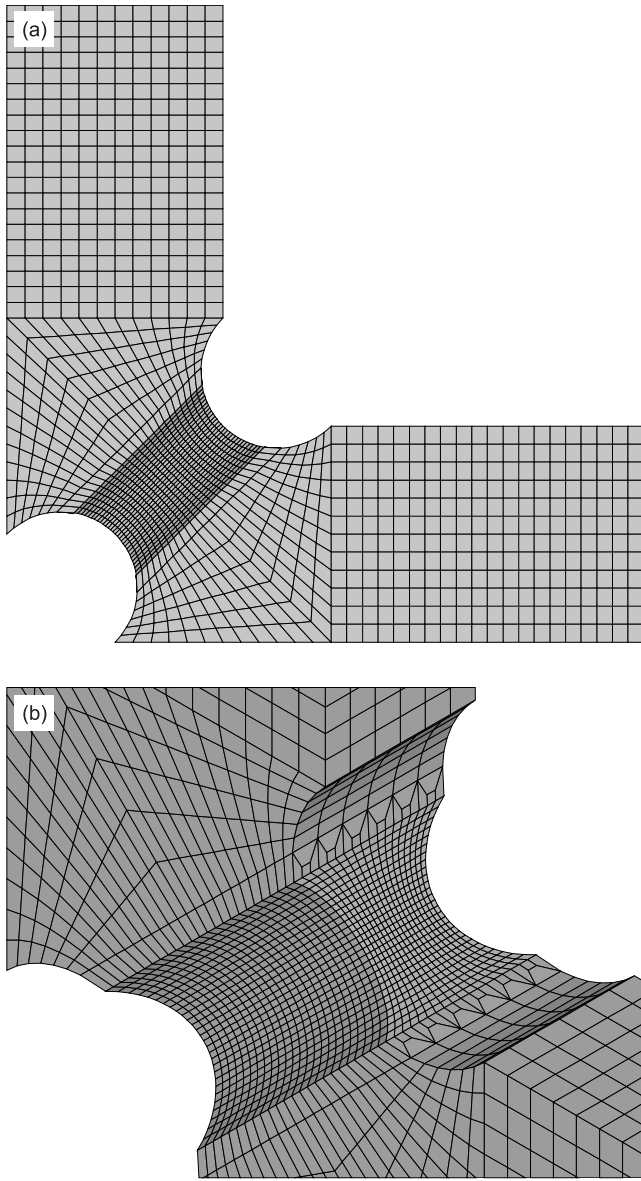
Fig. 4. Meshes of the X0-specimen: (a) overview and (b) details of the notched part.

where n is the total number of data points for each test, and F^{exp} and F^{sim} are the measured and numerically predicted forces, respectively. The respective values of $\bar{r}(F)$ are shown in Table 6, and it can be observed that the mean errors between the experimental and numerical simulations are less than 0.03, indicating very high accuracy in the global load–displacement curves. Moreover, when comparing the measured fracture forces $F_2^{\mathrm{fr,exp}}$ and the simulated fracture forces $F_2^{\mathrm{fr,sim}}$, the relative error for most of the loading cases is again below 0.03. However, the relative errors for the fracture forces in the X0-cyc-(1/-1)-0.65 and X0-cyc-(1/-1)-0.55 experiments are slightly higher than in the others. This is assumably due to the significant decrease in re-yielding stress observed in the failure loading pattern. In addition, it is observed that the experimental maximum $F_2^{\mathrm{max,exp}}$ and minimum $F_2^{\mathrm{min,exp}}$ forces along axis 2 exhibit slight differences, with the absolute values of $F_2^{\mathrm{max,exp}}$ being smaller than those of $F_2^{\mathrm{min,exp}}$. The maximum and minimum forces in each loading cycle also show no significant differences due to the symmetric machine displacements applied during the cyclic loading patterns. In addition, the absolute force value at the re-yielding point is lower than the absolute value at the previous reverse point under cyclic loading conditions. These observations suggest

the presence of the Bauschinger effect.

As the fracture forces F_2^{fr} summarized in Table 6, the specimen may fail under either tensile or compressive loading, with no apparent pattern. It reveals the randomness of specimen failure under different cyclic loading patterns. Additionally, the fracture forces for the X0-cyc-(1/-1)-0.80 and X0-cyc-(1/-1)-0.55 tests are noticeably lower than the others, as the failure occurred just after re-yielding or when significant force degradation had already occurred in the previous loading cycle. As the positive maximum force in axis 2 for the experiment X0-cyc-(1/-1)-0.55 decreases from the last tensile loading pattern to the previous tensile loading pattern, from $3.55\,\mathrm{kN}$ to $3.48\,\mathrm{kN}$, the degradation is evidently greater than in other loading patterns. The same phenomenon is observed under the loading case X0-cyc-(1/-1)-0.65, where the maximum tensile force decreases from $3.57\,\mathrm{kN}$ to $3.49\,\mathrm{kN}$. Based on this macroscopic observation, it may be concluded that a sudden drop in maximum force or re-yielding stress in just one loading pattern preceding failure or within the failure loading pattern is an essential indicator of specimen failure.

Furthermore, as shown in Fig. 5 and Table 6, different preloading ranges result in varying numbers of loading cycles before failure, such as half a cycle for the loading pattern X0-cyc-(1/-1)-1.2 and eight and a half cycles for the X0-cyc-(1/-1)-0.55 test. Note that if the loading direction along axis 2 changes twice, it is counted as one loading cycle. As shown in Figs. 5 (b)–(f), the relative displacements Δu_{ref} for each loading cycle are quite similar and nearly symmetric in both the tensile and compressive directions, due to the symmetric machine displacements imposed during cyclic loading patterns. The comparison of experimental load–displacement curves until the first unloading and the monotonic curve is illustrated in Fig. 6. The experimentally measured relative displacement ratio κ^{exp} for cyclic loading conditions is defined as the ratio of the relative displacement $\Delta u_{\mathrm{ref,2}}^{\mathrm{RP1}}$ at RP1 to the monotonic fractured relative displacement $\Delta u_{\mathrm{ref,2}}^{\mathrm{FP1}}$. The ratios are 0.92, 0.77, 0.62, 0.50, and 0.42 for the cyclic loading with increasing cycles, respectively. It can be observed that the relative displacements $\Delta u_{\mathrm{ref,2}}$ differ from the imposed machine displacements u_2^M, and thus, the experimentally measured relative displacement ratios κ^{exp} differ from the machine displacement ratios κ^M, as seen by comparing Tables 4 and 6.

In addition, a visibly deformed and undeformed X0-flower (outlined in red) is shown in Fig. 7, where the middle X0-flowers extend significantly along the vertical direction in the X0-cyc-(1/-1)-1.0 and X0-cyc-(1/-1)-1.2 experiments due to the applied positive loading. The corresponding experimentally measured maximum effective equivalent strain (von Mises), $\varepsilon_{\mathrm{eq}}^{\mathrm{exp}}$, values are 0.92 and 0.72, respectively, confirming that extremely large prestrains were applied. Although the loading conditions X0-cyc-(1/-1)-0.8, X0-cyc-(1/-1)-0.65, and X0-cyc-(1/-1)-0.55 show slight deformation compared to the red contour in Figs. 7(d)–(f), the maximum values of $\varepsilon_{\mathrm{eq}}^{\mathrm{exp}}$ measured in DIC are 0.45, 0.31, and 0.22, respectively.

A comparison of the experimentally measured and numerically predicted first principal strains A_1 just before failure on the notch surfaces is depicted in Fig. 8. The numerical results agree well with the experimental ones in both shear band distributions and maximum values. It is evident that the first principal strain $A_1 = 0.70$ under monotonic loading is significantly higher than those under cyclic loading patterns. Because the change in loading direction for cyclic loading alters the strain state, it results in different maximum values of first principal strains A_1. For example, experiment X0-cyc-(1/-1)-1.2 failed just before reaching the next reverse point (with around 1% deviation from the designed machine displacement of 1.2 mm), leading to a smaller maximum value and a broader shear band distribution. Additionally, noticeable distortion can be observed at the notched edge under monotonic loading (Fig. 8(a)) compared to other cyclic loading cases. Also, the X0-cyc-(1/-1)-0.65 and X0-cyc-(1/-1)-0.55 experiments show a highly discontinuous shear band, shaped like an X. In addition, the numerically predicted accumulated equivalent plastic strains γ are
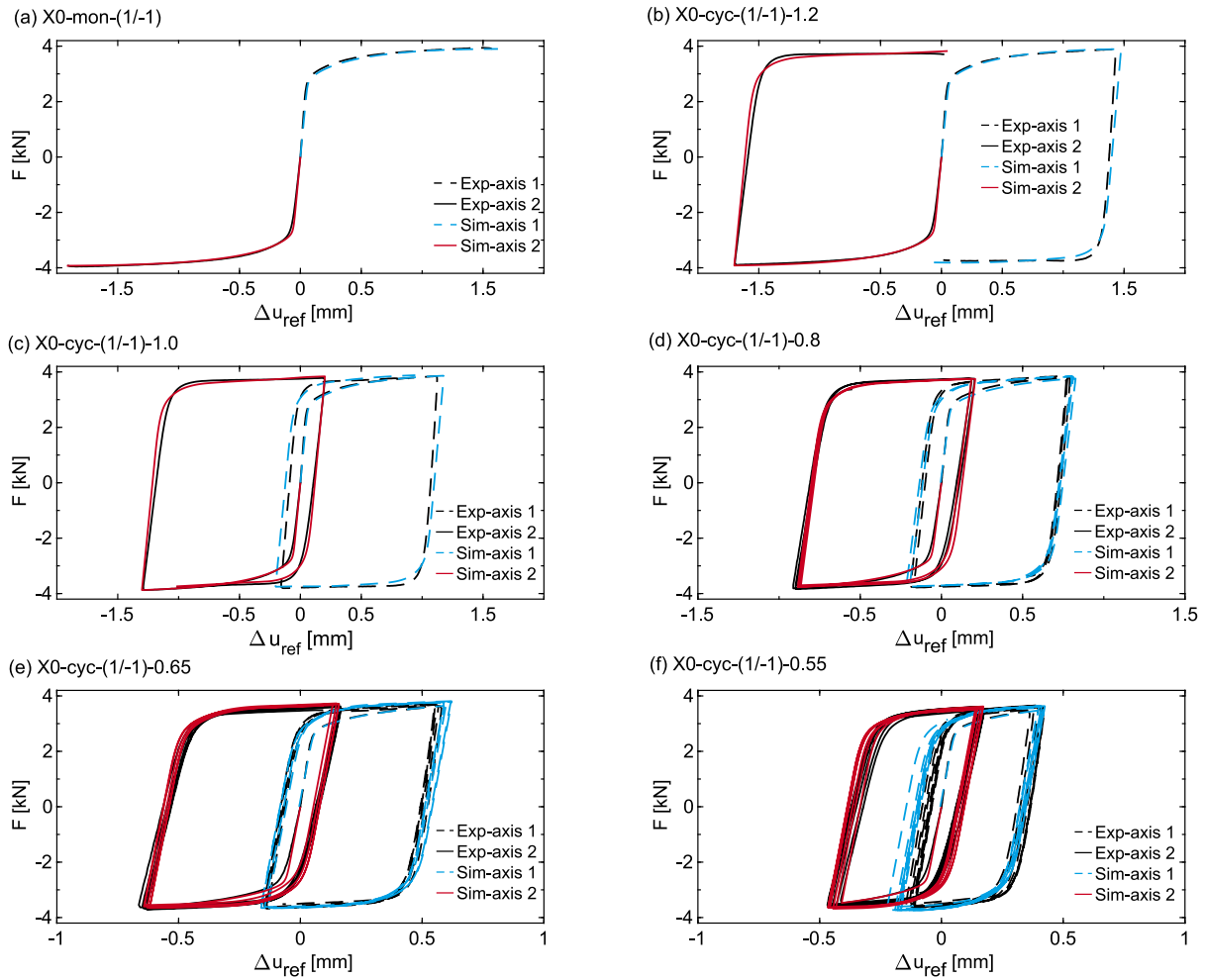
Fig. 5. Experimentally measured and numerically predicted load–displacement curves.

Table 6
Overview of experimental and simulated data based on global load–displacement curves.

Tests	$\Delta u_{\mathrm{ref},2}^{\mathrm{FP1/RP1}}$ [mm]	κ^{exp} [−]	N_{f} [−]	$\bar{r}(F)$ [−]	$F_2^{\mathrm{max,exp}}$ [kN]	$F_2^{\mathrm{min,exp}}$ [kN]	$F_2^{\mathrm{fr,exp}}$ [kN]	$F_2^{\mathrm{fr,sim}}$ [kN]	$r(F_2^{\mathrm{fr}})$ [−]
X0-mon-(1/-1)	−1.91	1	0	0.007	n/a	−3.96	−3.92	−3.93	0.002
X0-cyc-(1/-1)-1.2	−1.69	0.92	0.5	0.017	3.74	−3.90	3.70	3.82	0.030
X0-cyc-(1/-1)-1.0	−1.29	0.77	1	0.020	3.78	−3.88	−3.76	−3.74	0.005
X0-cyc-(1/-1)-0.8	−0.91	0.62	2.5	0.029	3.77	−3.84	3.37	3.48	0.021
X0-cyc-(1/-1)-0.65	−0.62	0.50	5	0.025	3.64	−3.71	3.49	3.65	0.046
X0-cyc-(1/-1)-0.55	−0.41	0.42	8.5	0.028	3.61	−3.66	−3.10	−3.31	0.073

shown in Fig. 9. One can observe that the equivalent plastic strains γ increase with the number of loading cycles N_{f}, while the angles between the plastic strain bands and the vertical directions become smaller. Moreover, the equivalent plastic strains γ on the notched cross-sections first appear at the middle of the notched edges and then spread along the edge with increasing γ. The above findings highlight how the loading paths and histories affect the local strain states.

5.2. Damage analysis

The damage strain tensor $\mathbf{A}^{\mathrm{da}}$ describes the volume and shape change of the micro-defects. The first principal damage strains A_1^{da} on notch surfaces and notched cross-sections are illustrated in Figs. 10(a)–(f) to characterize the damage behavior under different cyclic loading conditions.

Different damage distributions and maximum values are numerically predicted for various cyclic loading patterns. Although high-speed

cameras were not used during the experiments, crack lines can be clearly detected by comparing the images shortly before failure in some cases, as illustrated in Figs. 10(g)–(h). In most loading cases, the cracks occur in the middle of the notch surfaces, which is consistent with the numerical prediction of the damage shear band. Moreover, the maximum first principal damage strain $A_1^{\mathrm{da}} = 0.36\%$ appears on the top edge of the notch surface, where a visible crack initiation is also observed in Fig. 10(h) for the X0-cyc-(1/-1)-1.0 experiment. Additionally, the final fracture lines are shown in Fig. 11. The fracture lines align with the experimental and numerical shear bands, and fractures are observed at varying angles.

By comparing the first principal damage strain A_1^{da}, the maximal value under monotonic loading is greater than that under X0-cyc-(1/-1)-1.2 loading condition. As shown in the global load–displacement curves in Figs. 5(a) and (b), the X0-cyc-(1/-1)-1.2 changes the loading direction at the relative displacement $\Delta u_{2,\mathrm{ref}} = -1.68$ mm, and the same values and distributions are predicted at this reverse point in both
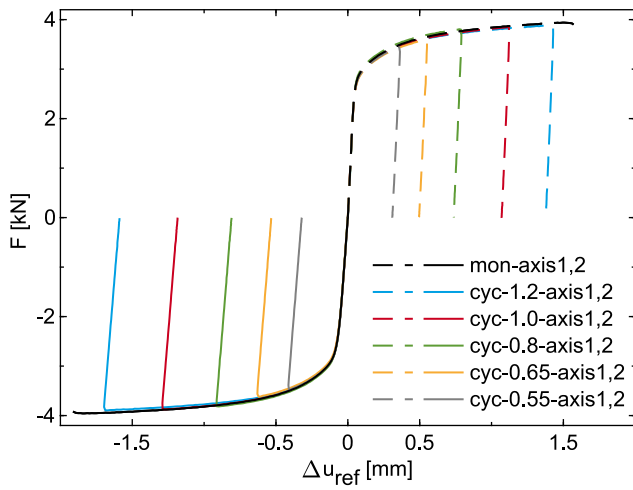
Fig. 6. Experimentally measured load–displacement curves up to the first reversal point (RP1) under cyclic loading and up to the fracture point (FP) under monotonic loading.
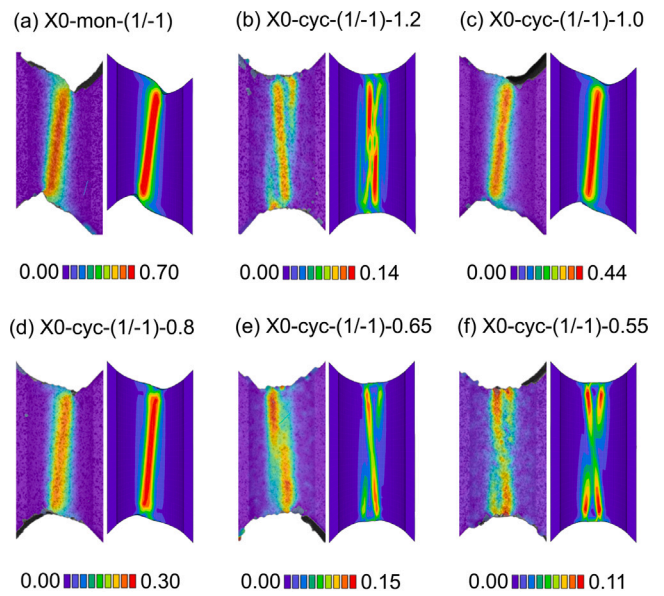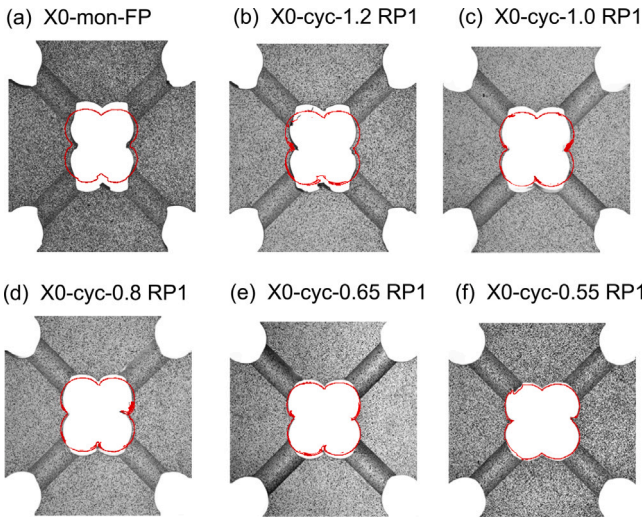

Fig. 7. Deformed and undeformed (marked with red contour) X0-flowers. Note that FP means fracture point, and RP1 represents the first reverse point.

Fig. 8. The experimentally measured and numerically predicted first principal strains A_1 on the notch surfaces.

Fig. 9. Numerically predicted the equivalent plastic strains γ on the notch surfaces and notched cross-sections.

loading cases. In addition, Wei et al. (2023a, 2024a) analyzed various shear reverse tests and concluded that micro-shear-cracks develop in the opposite direction after the reverse point (RP). Thus, the X0-cyc-(1/-1)-1.2 experiment has a smaller value of the first principal damage strain than monotonic loading. Notably, the maximum values occur at both the top and bottom edges of the notch surface for the X0-cyc-(1/-1)-1.2 experiment, where the fracture lines are also observed, as depicted in Fig. 11(b). This finding further confirms the accuracy of the numerical predictions of the damage.

Moreover, with increasing loading cycles, the maximum values of the first principal damage strain tend to increase until $N_f = 2.5$ cycles (loading case X0-cyc-(1/-1)-0.8) are applied, after which they begin to decrease. A similar trend is also observed for the first principal strain A_1, as shown in Figs. 8(d)–(f), revealing that different strain paths affect the damage behavior. In addition, the numerical simulations predict that damage occurs during the preloading stage for experiments X0-cyc-(1/-1)-1.2, X0-cyc-(1/-1)-1.0, and X0-cyc-(1/-1)-0.8, whereas damage appears later in the loading patterns X0-cyc-(1/-1)-0.65 and X0-cyc-(1/-1)-0.55. A smaller loading range results in a delayed occurrence of damage, as shown by the numerical simulations.
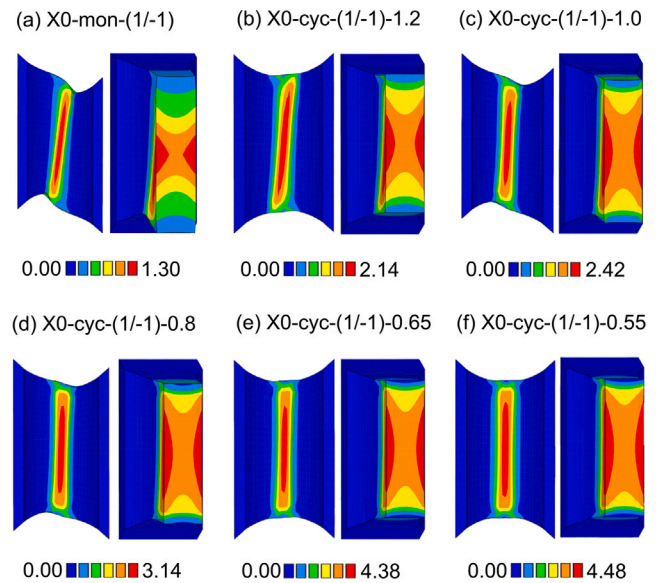
For monotonic loading conditions, the numerically predicted damage shows an increasing tendency throughout the entire loading process. However, the value may slightly decrease after the loading direction changes, indicating that cracks develop in a different direction. Based on the numerical simulations, the maximum first principal damage strain increases monotonically up to half the loading cycles of the X0-cyc-(1/-1)-0.65 and X0-cyc-(1/-1)-0.55 loading conditions, after which the increase becomes slower. As also reported by Algarni et al. (2019), the numerical analysis reveals that damage may occur and develop rapidly in the early cycles, then evolve more slowly.

To better quantitatively analyze the influence of damage under different loading conditions, damage strain invariants are introduced
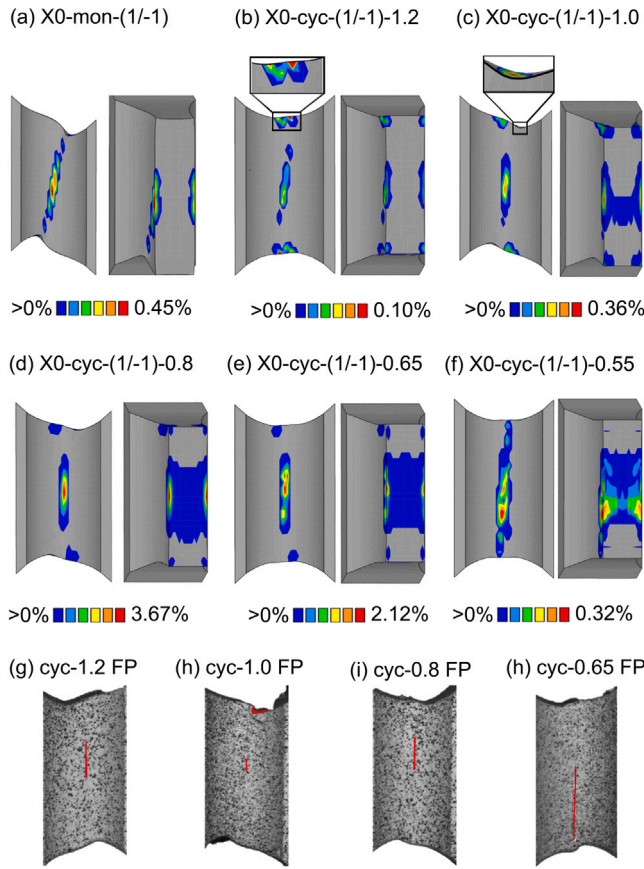
Fig. 10. Numerically predicted first principal damage strain A_1^{da} on the notch surfaces and notched cross-sections (a)–(f) and experimentally observed cracks just before failure (FP) on the notch surfaces in DIC.
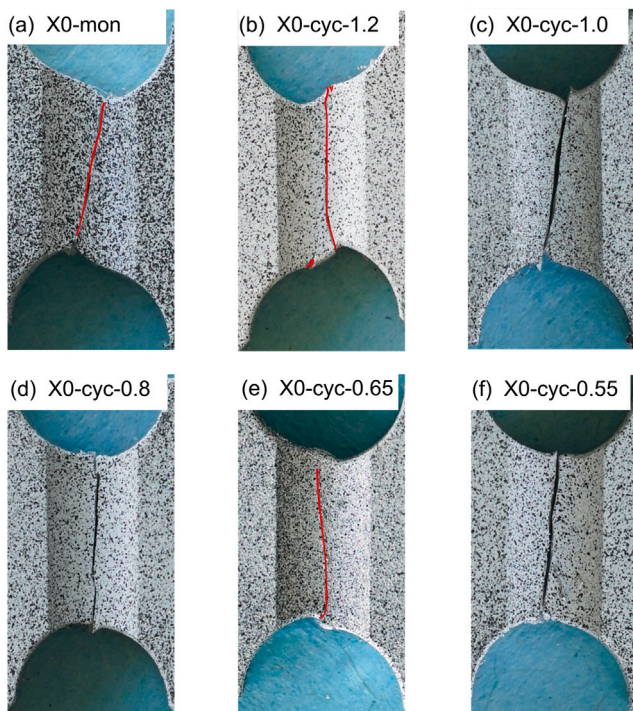

Fig. 11. Fracture images and fracture lines are marked in red in (a), (b), and (e).

Table 7
Damage stress invariants for the respective critical elements.

Tests	N_f	η	ω	I_1^{da}	$\sqrt{J_2^{da}}$	$\sqrt[3]{J_3^{da}}$	μ_{max}
mon	0	−0.04	0.07	0.0000	0.0136	−0.0050	0.022
cyc-1.2	0.5	−0.04	0.22	0.0000	0.0041	−0.0033	0.004
cyc-1.0	1	0.06	−0.15	0.0000	0.0109	0.0073	0.012
cyc-0.8	2.5	0.02	−0.05	0.0005	0.0492	0.0089	0.085
cyc-0.65	5	0.01	−0.01	0.0006	0.0256	0.0042	0.073
cyc-0.55	8.5	0.01	0.00	0.0000	0.0194	−0.0054	0.026

as follows:

$$I_1^{da} = \text{tr} \mathbf{A}^{da},$$

$$J_2^{da} = \frac{1}{2} \text{dev} \mathbf{A}^{da} \cdot \text{dev} \mathbf{A}^{da}, \qquad (20)$$

$$J_3^{da} = \det(\text{dev} \mathbf{A}^{da}),$$

where I_1^{da} describes the volume change of the micro-defects, J_2^{da} represents the isochoric deformation of the micro-defects, and J_3^{da} means the distortion of the micro-defects. In this work, the element with the maximum equivalent damage strain μ, integrated over the loading history of the equivalent damage strain rate $\dot{\mu}$ (Eq. (10)), is defined as the criterion for identifying the critical element in the numerical simulations in order to analyze the damage tensor under different cyclic loading patterns. As shown in Table 7, the stress triaxiality η and the Lode parameter ω are near zero, except for $\omega = 0.22$ and $\omega = -0.15$ under the cyclic loading patterns X0-cyc-(1/-1)-1.2 and X0-cyc-(1/-1)-1.0, respectively, where the maximum equivalent damage strain μ_{max} appears on the edge of the notched surface, as seen in the distribution of the first principal strain A_1^{da} in Figs. 10(b) and (c).

By comparing the magnitudes of the first, second, and third damage strain invariants, it is clear that the second damage strain invariant plays a more significant role than the other variables. From the numerical perspective, the damage is caused by the deformation of micro-shear-cracks under the present designed loading paths. Furthermore, the analysis of the second damage strain invariant $\sqrt{J_2^{da}}$ shows a similar tendency to the first principal damage strain across various cyclic loading conditions, with values increasing up to loading cycles $N_f = 2.5$ and then decreasing. Although in most loading cases, the magnitude of the third damage strain invariant $\sqrt[3]{J_3^{da}}$ is only $1/10$ of the $\sqrt{J_2^{da}}$ values, this small value still influences the deformation direction of micro-defects under low stress triaxialities. It can be observed that the value of $\sqrt[3]{J_3^{da}}$ changes from negative to positive up to $N_f = 2.5$ and then decreases back to negative. Compared to the first damage strain invariant I_1^{da}, it can be concluded that $\sqrt[3]{J_3^{da}}$ is more sensitive to shear-dominated damage mechanisms. One of the interesting numerical predictions is that the first damage strain invariant I_1^{da} is zero over most areas of the notch surface; however, a small value in the order of 10^{-4} appears at the center of the notch surface. The explanation is that during cyclic loading, the variation of loading in axes 1 and 2 from 1/-1 to −1/1 induces a small positive stress state in the middle of the notch, resulting in a non-zero I_1^{da}. As an example, the critical elements for the experiments X0-cyc-(1/-1)-0.8 and X0-cyc-(1/-1)-0.65 are observed at the center of the notched surface with I_1^{da} values of 0.0005 and 0.0006, respectively, as shown in Table 7. In addition, they failed under the loading condition on axis 1 with imposed negative loads, i.e., a loading ratio of −1/1, as shown in Fig. 5.

Although no clear and simple mathematics rules can be summarized from the damage strain variables under cyclic loading conditions, it is evident that the proposed approach provides valuable information about the influence of loading conditions and stress states. To accurately formulate fracture behavior, it is essential to consider all three invariants.
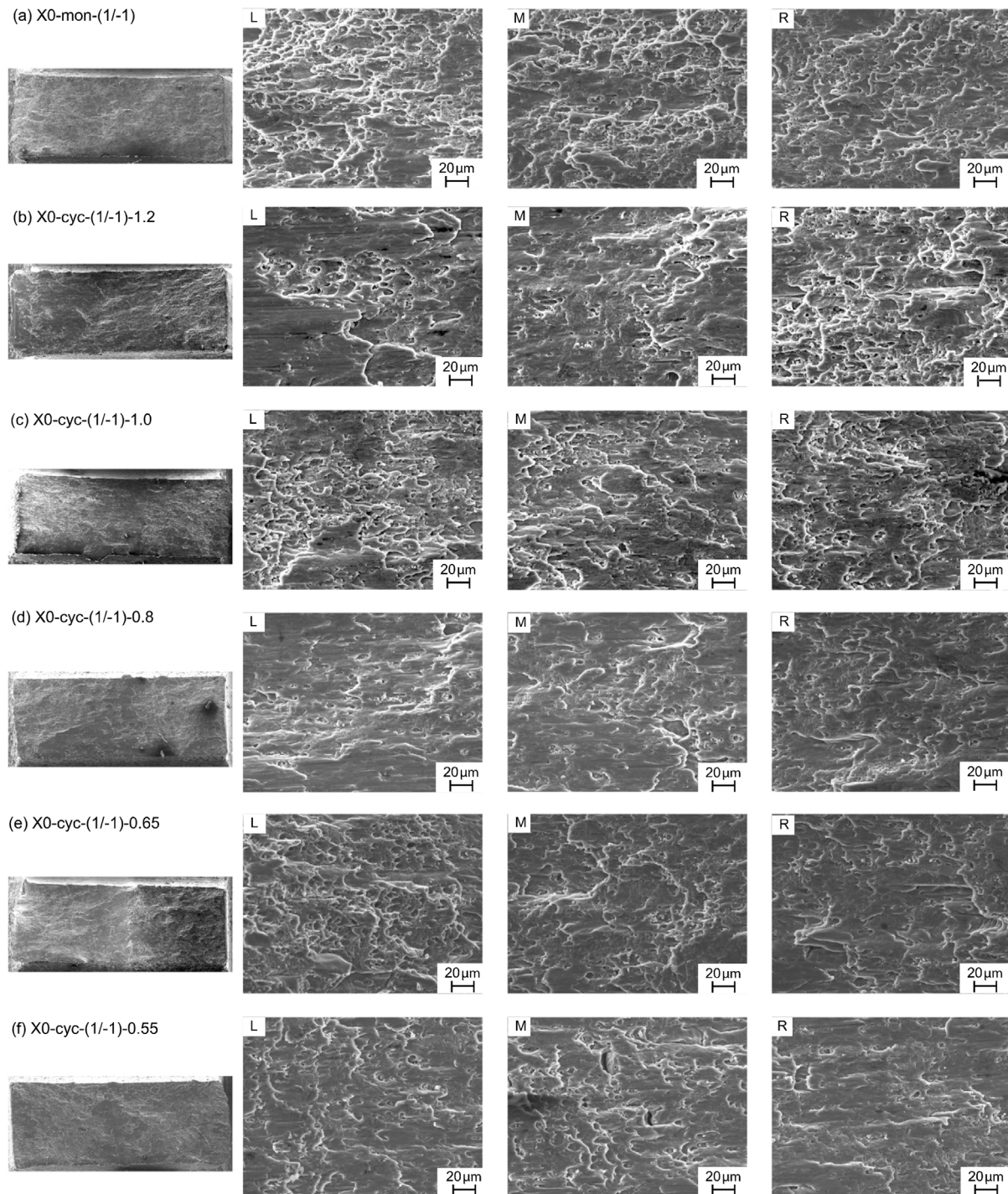
(a) X0-mon-(1/-1)

(b) X0-cyc-(1/-1)-1.2

(c) X0-cyc-(1/-1)-1.0

(d) X0-cyc-(1/-1)-0.8

(e) X0-cyc-(1/-1)-0.65

(f) X0-cyc-(1/-1)-0.55

Fig. 12. SEM images for the fracture surfaces on the notched cross-sections.

5.3. SEM images

Scanning electron microscopy (SEM) images were taken from the fracture surfaces of different experiments. For each loading case, an overview of the fracture surface and three positions (right, middle, and left) at a magnification of 500X were captured to study the details of the SEM images more closely, as illustrated in Fig. 12. In addition, the Canny edge detector (Canny, 1986; Gebäck and Koumoutsakos, 2009) in MATLAB is used to characterize crack boundaries based on sharp changes in pixel intensities. This work focuses on characterizing the total number of cracks N_{crack}, the average crack length l_{crack}, crack area density ρ_{area}, and crack length density ρ_{length}. Although the aspect ratio

and eccentricity can be used to analyze the shape of micro-defects and distinguish between micro-voids and micro-cracks, the lack of depth information for the micro-defects can lead to errors in classifying different types. In addition, the SEM images in Fig. 12 indicate that micro-shear-cracks primarily cause ductile damage. Also, the numerically predicted mean stress triaxialities $\bar{\eta} \approx 0$ and mean Lode parameter $\bar{\omega} \approx 0$ (see Table 8) across the notched cross-sections suggest that the current loading is shear-dominated, resulting in a shear-dominated damage mechanism. Therefore, in this study, the classification of micro-defects is not included in the statistical analysis.

Cyclic loading with a large strain range evidently induces ductile damage, as illustrated in Fig. 12. However, visually distinguishing the

Table 8
Crack characterization based on SEM image analysis.

Tests	N_f	$\bar{\eta}$	$\bar{\omega}$	$N_{\text{crack}} \pm \Delta N_{\text{crack}}$	$l_{\text{crack}} \pm \Delta l_{\text{crack}}$ [μm]	$\rho_{\text{area}} \pm \Delta \rho_{\text{area}}$ [μm²/μm²]	$\rho_{\text{length}} \pm \Delta \rho_{\text{length}}$ [μm/μm²]
mon	0	0.03	−0.04	17223 ± 767	0.1866 ± 0.0066	0.1074 ± 0.0029	10.2090 ± 0.1884
cyc-1.2	0.5	0.01	−0.04	17920 ± 2408	0.1744 ± 0.0090	0.1055 ± 0.0122	9.9011 ± 0.8962
cyc-1.0	1	0.02	−0.03	18043 ± 1326	0.1778 ± 0.0051	0.1056 ± 0.0070	10.1898 ± 0.5111
cyc-0.8	2.5	0.00	−0.01	20324 ± 2366	0.1696 ± 0.0118	0.1178 ± 0.0107	10.9092 ± 0.6350
cyc-0.65	5	0.01	−0.03	18939 ± 1718	0.1707 ± 0.0050	0.1101 ± 0.0127	10.2638 ± 0.6440
cyc-0.55	8.5	−0.01	0.03	20246 ± 1540	0.1658 ± 0.0054	0.1137 ± 0.0089	10.6646 ± 0.5583

differences between various loading conditions is difficult. Since the software overlaps the overview of the fracture surface and provides a lower resolution, the mean values from SEM images at three different positions (right, middle, and left) for each loading case are used to analyze the micro-defect behavior. The mean values and respective standard deviations from the analysis of the SEM images are summarized in Table 8. It can be observed that the mean crack length l_{crack} shows a decreasing trend with increasing loading cycles. This observation confirms that the micro-shear-cracks alter their development direction under cyclic loading, resulting in shorter cracks. The predicted damage strain tensor also demonstrates this same tendency, changing direction and magnitude, as observed in the numerical simulations Fig. 10. The crack area density ρ_{area} and crack length density ρ_{length} correlate with damage; higher values indicate more significant damage. Both densities show the same trend: initially increasing until reaching the loading case with a loading cycle of N_f = 2.5 (X0-cyc-(1/-1)-0.8), after which they decrease. Additionally, values for the loading patterns X0-cyc-(1/-1)-1.2 and X0-cyc-(1/-1)-1.0 are smaller than those under monotonic loading, whereas values under other cyclic loading patterns are greater than those under monotonic loading. This observation aligns with the proposed damage model, which predicts the tendency of the maximum principal damage strain A_1^{da}, as shown in Fig. 10. It highlights that the numerical simulation of damage prediction closely matches the experimental results.

6. Conclusion

The novel biaxially loaded shear cyclic loading tests using X0-specimens were performed with different numbers of loading cycles under large strain ranges. A loading ratio of 1/-1, i.e., equal magnitudes of positive and negative forces applied along different loading axes, results in a stress triaxiality and Lode parameter close to zero, with a maximum value of 0.04. This provides an ideal loading pattern for studying shear damage mechanisms under various cyclic loading conditions. Analysis of the scanning electron microscopy images of the fracture surfaces confirmed that micro-shear-cracks, resulting in ductile damage, are the primary cause of failure under the present design of extremely low-cycle shear cyclic loading. Moreover, the Canny edge detector is used to characterize the boundaries of the micro-defects, and statistical analysis shows that the mean crack length is larger under monotonic loading than under cyclic loading conditions. However, the crack density for cyclic loading with a loading number N_f greater than 2.5 is higher than under monotonic loading conditions, indicating that material degradation is more severe under more cyclic loading. These findings highlight the influence of the number of loading cycles at the micro-level.

The advanced anisotropic continuum damage model is used for numerical calculations, and numerical simulations agree well with the experimental results at both the global load–displacement and local strain fields. The errors between the measured and predicted load–displacement values are all below 3%, indicating a very high accuracy of the proposed material model. An analysis of the experimental and numerical first principal strain fields reveals how the loading patterns affect the strain field distribution and magnitude. One of the highlights is the proposed anisotropic damage strain tensor. The distribution of the damage strain is consistent with the crack initiation and fracture

lines. The changing trend of the maximum principal damage strain for different loading conditions aligns with the crack density of the micro-shear-cracks. In addition, the numerical damage predictions reveal that the damage occurs in the early cycles and increasingly slowly in the rest of the loading cycles. Additionally, the micro-shear-cracks may change their development direction with changes in loading direction, as confirmed by the mean crack length in the SEM analysis. The findings mentioned above demonstrate that the present damage model provides effective information that cannot be directly measured in experiments.

CRediT authorship contribution statement

Zhichao Wei: Writing – original draft, Visualization, Software, Methodology, Investigation, Formal analysis, Data curation, Conceptualization. **Marleen Harting:** Writing – review & editing, Validation, Investigation, Data curation. **Steffen Gerke:** Writing – review & editing, Validation, Methodology, Investigation, Conceptualization. **Michael Brünig:** Writing – review & editing, Supervision, Resources, Project administration, Methodology, Funding acquisition, Conceptualization.

Declaration of competing interest

The authors declare that they have no known competing financial interests or personal relationships that could have appeared to influence the work reported in this paper.

Data availability

Data will be made available on request.

References

Abu Al-Rub, R.K., Voyiadjis, G.Z., 2003. On the coupling of anisotropic damage and plasticity models for ductile materials. Int. J. Solids Struct. 40, 2611–2643.

Algarni, M., Bai, Y., Zwawi, M., Ghazali, S., 2019. Damage evolution due to extremely low-cycle fatigue for Inconel 718 alloy. Metals 9 (1109).

Bao, Y., Wierzbicki, T., 2004. On fracture locus in the equivalent strain and stress triaxiality space. Int. J. Mech. Sci. 46, 81–98.

Bao, Y., Wierzbicki, T., 2005. On the cut-off value of negative triaxiality for fracture. Eng. Fract. Mech. 72, 1049–1069.

Barlat, F., Ferreira Duarte, J.M., Gracio, J.J., Lopes, A.B., Rauch, E.F., 2003. Plastic flow for non-monotonic loading conditions of an aluminum alloy sheet sample. Int. J. Plast. 19, 1215–1244.

Bouvier, S., Haddadi, H., Levée, P., Teodosiu, C., 2006. Simple shear tests: Experimental techniques and characterization of the plastic anisotropy of rolled sheets at large strains. J. Mater. Process. Technol. 172, 96–103.

Brosius, A., Yin, Q., Güner, A., Tekkaya, A.E., 2011. A new shear test for sheet metal characterization. Steel Res. Int. 82, 323–328.

Brünig, M., 2003. An anisotropic ductile damage model based on irreversible thermodynamics. Int. J. Plast. 19, 1679–1713.

Brünig, M., Chyra, O., Albrecht, D., Driemeier, L., Alves, M., 2008. A ductile damage criterion at various stress triaxialities. Int. J. Plast. 24, 1731–1755.

Brünig, M., Gerke, S., Hagenbrock, V., 2013. Micro-mechanical studies on the effect of the stress triaxiality and the lode parameter on ductile damage. Int. J. Plast. 50, 49–65.

Brünig, M., Gerke, S., Schmidt, M., 2016. Biaxial experiments and phenomenological modeling of stress-state-dependent ductile damage and fracture. Int. J. Fract. 200, 63–76.

Brünig, M., Gerke, S., Schmidt, M., 2018. Damage and failure at negative stress triaxialities: experiments, modeling and numerical simulations. Int. J. Plast. 102, 70–82.

Brünig, M., Koirala, S., Gerke, S., 2022. Analysis of damage and failure in anisotropic ductile metals based on biaxial experiments with the H-specimen. Exp. Mech. 62, 183–197.

Brünig, M., Zistl, M., Gerke, S., 2021. Numerical analysis of experiments on damage and fracture behavior of differently preloaded aluminum alloy specimens. Metals 11 (381).

Canny, J., 1986. A computational approach to edge detection. IEEE Trans. Pattern Anal. Mach. Intell. PAMI-8, 679–698.

Chaboche, J.L., 1992. Damage induced anisotropy: On the difficulties associated with the active/passive unilateral condition. Int. J. Damage Mech. 1, 148–171.

Cortese, L., Nalli, F., Rossi, M., 2016. A nonlinear model for ductile damage accumulation under multiaxial non-proportional loading conditions. Int. J. Plast. 85, 77–92.

Daroju, S., Kuwabara, T., Sharma, R., Fullwood, D.T., Miles, M.P., Knezevic, M., 2022. Experimental characterization and crystal plasticity modeling for predicting load reversals in AA6016-T4 and AA7021-t79. Int. J. Plast. 153, 103292.

Driemeier, L., Brünig, M., Micheli, G., Alves, M., 2010. Experiments on stress-triaxiality dependence of material behavior of aluminum alloys. Mech. Mater. 42, 207–217.

Dunand, M., Mohr, D., 2011. Optimized butterfly specimen for the fracture testing of sheet materials under combined normal and shear loading. Eng. Fract. Mech. 78, 2919–2934.

Faleskog, J., Barsoum, I., 2013. Tension–torsion fracture experiments—Part I: Experiments and a procedure to evaluate the equivalent plastic strain. Int. J. Solids Struct. 50, 4241–4257.

Gao, X., Zhang, G., Roe, C., 2010. A study on the effect of the stress state on ductile fracture. Int. J. Damage Mech. 19, 75–94.

Gebäck, T., Koumoutsakos, P., 2009. Edge detection in microscopy images using curvelets. BMC Bioinformatics 10 (75).

Gerke, S., Adulyasak, P., Brünig, M., 2017. New biaxially loaded specimens for the analysis of damage and fracture in sheet metals. Int. J. Solids Struct. 110–111, 209–218.

Gerke, S., Wei, Z., Brünig, M., 2024. Experiments on low–cycle ductile damage and failure under biaxial loading conditions. Exp. Mech..

Gurson, A.L., 1977. Continuum theory of ductile rupture by void nucleation and growth: Part I—yield criteria and flow rules for porous ductile media. J. Eng. Mater. Technol. 99, 2–15.

Hayakawa, K., Murakami, S., Liu, Y., 1998. An irreversible thermodynamics theory for elastic–plastic-damage materials. Eur. J. Mech. A Solids 17, 13–32.

Holmen, J.K., Frodal, B.H., Hopperstad, O.S., Børvik, T., 2017. Strength differential effect in age hardened aluminum alloys. Int. J. Plast. 99, 144–161.

Hou, Y., Lee, M.G., Lin, J., Min, J., 2022. Experimental characterization and modeling of complex anisotropic hardening in quenching and partitioning (Q & P) steel subject to biaxial non-proportional loadings. Int. J. Plast. 156, 103347.

Iftikhar, C.M.A., Khan, A.S., 2021. The evolution of yield loci with finite plastic deformation along proportional and non-proportional loading paths in an annealed extruded AZ31 magnesium alloy. Int. J. Plast. 143, 103007.

Kanvinde, A.M., Deierlein, G.G., 2007. Cyclic void growth model to assess ductile fracture initiation in structural steels due to ultra low cycle fatigue. J. Eng. Mech. 133, 701–712.

Khan, I.A., Benzerga, A.A., Needleman, A., 2023. A shear modified enhanced gurson constitutive relation and implications for localization. J. Mech. Phys. Solids 171, 105153.

Khan, A.S., Liu, H., 2012. A new approach for ductile fracture prediction on Al 2024-T351 alloy. Int. J. Plast. 35, 1–12.

Kong, X., Morgeneyer, T.F., Missoum-Benziane, D., Rousselier, G., 2023. A polycrystalline damage model applied to an anisotropic aluminum alloy 2198 under non-proportional load path changes. Int. J. Plast. 168, 103674.

Lemaitre, J., 1985. A continuous damage mechanics model for ductile fracture. J. Eng. Mater. Technol 107, 83–89.

Lian, J., Sharaf, M., Archie, F., Münstermann, S., 2013. A hybrid approach for modelling of plasticity and failure behaviour of advanced high-strength steel sheets. Int. J. Damage Mech. 22, 188–218.

Malcher, L., Andrade Pires, F.M., César de Sá, J., 2014. An extended GTN model for ductile fracture under high and low stress triaxiality. Int. J. Plast. 54, 193–228.

Marcadet, S.J., Mohr, D., 2015. Effect of compression–tension loading reversal on the strain to fracture of dual phase steel sheets. Int. J. Plast. 72, 21–43.

Mohr, D., Marcadet, S.J., 2015. Micromechanically-motivated phenomenological Hosford–Coulomb model for predicting ductile fracture initiation at low stress triaxialities. Int. J. Solids Struct. 67–68, 40–55.

Nahshon, K., Hutchinson, J.W., 2008. Modification of the Gurson model for shear failure. Eur. J. Mech. A Solids 27, 1–17.

Ohno, N., 1982. A constitutive model of cyclic plasticity with a nonhardening strain region. J. Appl. Mech. 49, 721–727.

Papasidero, J., Doquet, V., Mohr, D., 2015. Ductile fracture of aluminum 2024-T351 under proportional and non-proportional multi-axial loading: Bao–Wierzbicki results revisited. Int. J. Solids Struct. 69-70, 459–474.

Raj, A., Verma, R.K., Singh, P.K., Shamshoddin, S., Biswas, P., Narasimhan, K., 2022. Experimental and numerical investigation of differential hardening of cold rolled steel sheet under non-proportional loading using biaxial tensile test. Int. J. Plast. 154, 103297.

Shi, Y., Wang, M., Wang, Y., 2011. Experimental and constitutive model study of structural steel under cyclic loading. J. Constr. Steel Res. 67, 1185–1197.

Spitzig, W.A., Richmond, O., 1984. The effect of pressure on the flow stress of metals. Acta Metall. 32, 457–463.

Tvergaard, V., Needleman, A., 1984. Analysis of the cup-cone fracture in a round tensile bar. Acta Metall. 32, 157–169.

Voyiadjis, G.Z., Hoseini, S.H., Farrahi, G.H., 2012. Effects of stress invariants and reverse loading on ductile fracture initiation. Int. J. Solids Struct. 49, 1541–1556.

Voyiadjis, G.Z., Hoseini, S.H., Farrahi, G.H., 2013. A plasticity model for metals with dependency on all the stress invariants. J. Eng. Mater. Technol. 135, 011002.

Voyiadjis, G.Z., Kattan, P.I., 1999. Advances in Damage Mechanics: Metals and Metal Matrix Composites. Elsevier, Amsterdam, http://dx.doi.org/10.1016/C2009-0-13418-9.

Voyiadjis, G.Z., Kattan, P.I., 2005. Damage Mechanics. CRC Press, http://dx.doi.org/10.1201/9781420027839.

Voyiadjis, G.Z., Kattan, P.I., 2009. A comparative study of damage variables in continuum damage mechanics. Int. J. Damage Mech. 18, 315–340.

Weck, A., Wilkinson, D.S., 2008. Experimental investigation of void coalescence in metallic sheets containing laser drilled holes. Acta Mater. 56, 1774–1784.

Wei, Z., Gerke, S., Brünig, M., 2023a. Damage and fracture behavior under non-proportional biaxial reverse loading in ductile metals: Experiments and material modeling. Int. J. Plast. 171, 103774.

Wei, Z., Gerke, S., Brünig, M., 2023b. Mechanical responses of ductile aluminum alloy under biaxial non-proportional tensile reverse loading patterns. Metals 13 (1922).

Wei, Z., Gerke, S., Brünig, M., 2024a. Ductile damage and fracture characterizations in bi-cyclic biaxial experiments. Int. J. Mech. Sci. 109380.

Wei, Z., Gerke, S., Brünig, M., 2024b. Novel uniaxial and biaxial reverse experiments for material parameter identification in an advanced anisotropic cyclic plastic-damage model. Mech. Mater. 105294. http://dx.doi.org/10.1016/j.mechmat.2025.105294.

Wei, Z., Gerke, S., Brünig, M., 2024c. Numerical analysis of non-proportional biaxial reverse experiments with a two-surface anisotropic cyclic plasticity-damage approach. Comput. Methods Appl. Mech. Engrg. 419, 116630.

Wei, Z., Zistl, M., Gerke, S., Brünig, M., 2022. Analysis of ductile damage and fracture under reverse loading. Int. J. Mech. Sci. 107476.

Wei, Z., Zistl, M., Gerke, S., Brünig, M., 2023c. Analysis of ductile damage evolution and failure mechanisms due to reverse loading conditions for the aluminum alloy EN-AW 6082–T6. Proc. Appl. Math. Mech. 22.

Wu, H., Zhang, C., Yang, H., Zhuang, X., Zhao, Z., 2024. Extended Gurson-Tvergaard-Needleman model considering damage behaviors under reverse loading. Int. J. Mech. Sci. 272, 109196.

Wu, H., Zhuang, X., Zhao, Z., 2022. Extended GTN model for predicting ductile fracture under a broad range of stress states. Int. J. Solids Struct. 239–240, 111452.

Xue, Z., Faleskog, J., Hutchinson, J.W., 2013. Tension–torsion fracture experiments – Part II: Simulations with the extended gurson model and a ductile fracture criterion based on plastic strain. Int. J. Solids Struct. 50, 4258–4269.

Yoshida, F., Uemori, T., Fujiwara, K., 2002. Elastic–plastic behavior of steel sheets under in-plane cyclic tension–compression at large strain. Int. J. Plast. 18, 633–659.

Zeng, C., Fang, X., Habibi, N., Münstermann, S., Lian, J., 2024. A rate-dependent damage mechanics model for predicting plasticity and ductile fracture behavior of sheet metals at high strain rates. Eng. Fract. Mech. 306, 110217.

Zhang, J., Brepols, T., Reese, S., 2023. A two–surface damage–plasticity model based on a drucker—Prager yield criterion. Proc. Appl. Math. Mech 22.

Zhang, Q., Ritzert, S., Zhang, J., Kehls, J., Reese, S., Brepols, T., 2025. A multi-field decomposed model order reduction approach for thermo-mechanically coupled gradient-extended damage simulations. Comput. Methods Appl. Mech. Engrg. 434, 117535.

Zhou, J., Gao, X., Sobotka, J.C., Webler, B.A., Cockeram, B.V., 2014. On the extension of the gurson-type porous plasticity models for prediction of ductile fracture under shear-dominated conditions. Int. J. Solids Struct. 51, 3273–3291.

Zistl, M., Brünig, M., Gerke, S., 2022. Analysis of damage and fracture behavior in ductile metal sheets undergoing compression and shear preloading. Int. J. Mater. Form 15.